

Electronic Supporting Information

SERS and Plasmonic Heating Efficiency from Anisotropic Core/Satellite Superstructures

Christian Kuttner,^{*#a,b} Roland P. M. Höller,^{#c} Marta Quintanilla,^a Max J. Schnepf,^c
Martin Dulle,^d Andreas Fery,^{b,c,e} and Luis M. Liz-Marzán^{a,f}

^a CIC biomaGUNE, BioNanoPlasmonics Laboratory,
Paseo de Miramón 182, 20014 Donostia-San Sebastián, Spain.

^b Cluster of Excellence Center for Advancing Electronics Dresden (cfaed),
Technische Universität Dresden, Helmholtzstraße 18, 01069 Dresden, Germany.

^c Leibniz-Institut für Polymerforschung Dresden e.V. (IPF), Institute for Physical
Chemistry and Polymer Physics, Hohe Straße 6, 01069 Dresden, Germany

^d Jülich Centre for Neutron Science (JCNS-1), Institute for Complex Systems (ICS-1),
Forschungszentrum Jülich GmbH, Wilhelm-Johnen-Straße, 52428 Jülich, Germany.

^e Physical Chemistry of Polymeric Materials, Technische Universität Dresden,
Bergstraße 66, 01069 Dresden, Germany.

^f Ikerbasque, Basque Foundation for Science, 48013 Bilbao, Spain.

#These authors contributed equally.

*Corresponding author: ckuttner@cicbiomagune.es

Table of Content:

Section ESI.0: Materials and methods (page S2)

Section ESI.1: Experimental optical properties and electron microscopy (page S5)

Section ESI.2: Quantification of radiative and non-radiative losses (page S7)

Section ESI.3: Structural characterization and 3D SAXS modeling (page S8)

Section ESI.4: Electromagnetic simulations (page S11)

Section ESI.5: Plasmonic coupling of multi-satellite assemblies (page S12)

Section ESI.6: Analysis of SERS data and reference Raman spectra (page S16)

Section ESI.7: Calculation of the enhancement factor and surface coverage of NTP (page S17)

Section ESI.8: Plasmonic heating experiments (page S19)

ESI References (page S19)

Section ESI.0: Materials and methods

Materials. $\text{HAuCl}_4 \cdot 3\text{H}_2\text{O}$ ($\geq 99.9\%$), AgNO_3 (99.9999%), NaBH_4 (99.99%), hydroquinone (HQ, 99%), sodium citrate tribasic dihydrate ($\geq 99\%$), ascorbic acid ($\geq 99\%$, AA), CTAC (25% w/w, 756 mM), 4-nitrothiophenol (NTP, 99%) were purchased from Sigma-Aldrich. CTAB (99%) was purchased from Merck chemicals. Sodium hydroxide concentrate (0.1 M, NaOH) was purchased from Grüssing GmbH. Ethanol absolute ($\geq 98\%$) was purchased from VWR Chemicals. All chemicals were used as received. All solutions, except HAuCl_4 , were prepared immediately before use. Purified Milli-Q water was used in all experiments (Millipore, 18.2 M Ω cm). Glassware was cleaned with *aqua regia* and rinsed extensively with Milli-Q water before use.

Synthesis of nanospheres. Quasi-spherical citrate-capped AuNPs of 15 nm size were synthesized as reported recently.^{S1}

P(SS-co-MA)-coating of NPs via ligand-exchange. The citrate-capped AuNPs were coated with a solution of P(SS-co-MA) using a ligand-exchange process previously reported by Karg *et al.*^{S2} 40 mL of citrate-stabilized AuNPs (0.5 mM Au^0) was added dropwise to 10 mL of a 1 mg mL⁻¹ P(SS-co-MA) solution (6 mM NaCl) under vigorous stirring. The P(SS-co-MA)/NaCl solution was sonicated at least for 30 min before use. The NP dispersion was stirred over night at RT to ensure a complete ligand exchange. To remove the excess of unbound P(SS-co-MA), the NP dispersion was purified by 5 centrifugation steps (8000 rcf, 30 min). The precipitated NPs were redispersed in basic water (pH 9-10) after each centrifugation cycle. After the last cycle, the P(SS-co-MA)-coated AuNPs were directly used as building blocks for the assembly of superstructures.

Synthesis of nanorods. Seed Synthesis: CTAB solution (5 mL, 0.2 M) was mixed with 5 mL of an aqueous 0.5 mM HAuCl_4 solution (23.27 μL of a 0.10742 M HAuCl_4 solution was added to 5 mL of water). 600 μL of 0.01 M NaBH_4 solution was quickly added while stirring vigorously, resulting in a brownish yellow solution. Stirring was continued for 2 min, then the seed solution was kept at RT for up to 30 min until use. AuNR growth: 12.76 g CTAB was dissolved in 350 mL of purified water (f.c.: 0.1 M). 1.629 mL of 0.10742 M HAuCl_4 solution (f.c.: 0.5 mM) and 350 μL of 0.1 M AgNO_3 solution were added (f.c.: 0.1 mM). After at least 5 min, 17.5 mL of 0.1 M HQ solution (f.c.: 5 mM) was added while stirring. 2 min later, 8.4 mL of the as-prepared seed solution was added. Before further use, the AuNR suspension was kept at 32 °C for at least 48 h.

MUTAB-functionalization of NPs via ligand-exchange. Before functionalization with MUTAB, a ligand exchange from CTAB to CTAC was done by several centrifugation/redispersion cycles to ensure a full surfactant replacement.^{S3} Though this functionalization does not appear to be sensitive toward the counter-ions, the use of CTAC is preferable to avoid crystallization of CTAB at low temperatures. The CTAC-capped AuNRs were coated with MUTAB using a ligand-exchange process, as previously reported.^{S4} 40 mL of CTAC-stabilized AuNRs (0.25 mM Au^0 , 1 mM CTAC) was added dropwise to 10 mL of a 1 mg mL⁻¹ MUTAB solution under vigorous stirring at RT. The stirring was continued overnight to ensure a complete ligand exchange. The 5 centrifugation steps (1000-4000 rcf, 10-20 min) were performed to remove the excess of unbound MUTAB and CTAC. After the first centrifugation cycle, the precipitated NPs were redispersed without ultrasound in a 0.1 mg mL⁻¹

MUTAB solution. In the following 4 cycles, neutral water (pH 7) was used. After the last cycle, the MUTAB-capped AuNRs were directly used as building blocks for the assembly of superstructures.

Self-assembly of superstructures. In a glass vial, 500 μL of MUTAB-coated core NPs (1×10^9 NPs mL^{-1}) was added in one shot to 500 μL of fivefold purified and concentrated P(SS-co-MA)-coated satellite NPs (1×10^{12} NPs mL^{-1}) under vigorous stirring (core-to-satellite ratio 1:1000). Before the assembly, the satellite NPs were dispersed in a 12 mM NaCl solution (pH 7). The NP/superstructure dispersion was stirred at least for 1 min. After the assembly, the nanocluster dispersion was added dropwise to 1 mL of 0.1 mg mL^{-1} P(SS-co-MA) solution (6 mM NaCl). Then, the nanoclusters were purified by 4 centrifugation/redispersion cycles (to remove excess of free satellite NPs) using basic water (pH 9-10).

NTP labeling. Equimolar sample solutions were prepared from aliquots of nanoclusters dispersions ($[\text{Au}^0] = 0.25$ mM) and aqueous analyte solutions ($[\text{NTP}] = 1$ μM). Briefly, the dispersions of nanoclusters and building blocks were set to 0.25 mM Au^0 using UV/vis/NIR spectroscopy. Afterward, 5 μL of a 101.0 μM NTP in EtOH solution was added to 500 μL of the adjusted nanocluster solutions, for a final NTP in $\text{H}_2\text{O}/\text{EtOH}$ concentration of 1.0 μM . After the addition of the analyte molecules, SERS measurements were taken after certain time intervals. A complete adsorption of NTP could be observed after about 1 day.

Electron microscopy. TEM images were obtained using a Zeiss Libra 120 with an accelerating voltage of 120 kV. Samples were prepared by placing a 2 μL droplet of diluted (nearly colorless) NP dispersions on TEM grids (Cu, 200 Mesh, coated with carbon film; Science Services GmbH). SEM images were obtained using a Zeiss NEON40 equipped with a field-emission cathode with an operating voltage of 3 kV. Samples were prepared by placing a 2 μL droplet of the diluted NP dispersions on silicon wafers (Sigma-Aldrich). The silicon wafers were cleaned with Milli-Q water before use and attached on Al pin stubs (Plano GmbH) using a conductive adhesive film.

Optical characterization. Spectra were acquired with an UV/vis/NIR spectrophotometer Cary 5000 (Agilent Technologies Deutschland GmbH). The extinction at the wavelength of 400 nm (interband transitions),^{S5} which is assumed to have a size-independent absorption coefficient,^{S6,S7} was used to normalize the UV/vis/NIR spectra and to calculate the molar concentration of Au^0 in the NP dispersions. The molar concentration of Au^0 and the size of the nanoparticles obtained from TEM images enabled the calculation of the particle concentration (number of AuNPs per volume). The absorption and scattering losses were determined using the external diffuse reflectance accessory 2500 (integrating sphere), as described elsewhere.^{S1}

SAXS. Scattering patterns were recorded with the SAXS system “Ganesha-Air” from (SAXSLAB, Xenocs). The X-ray source of this laboratory-based system was a D2-MetalJet (Excillum) with a liquid-metal anode operating at 70 kV and 3.57 mA with Ga- $K\alpha$ radiation ($\lambda = 0.1341$ nm) providing a very brilliant and a very small beam (<100 μm). The beam was focused with a focal length of 55 cm using a specially made X-ray optic (Xenocs) to provide a very small and intense beam at the sample position. Measurements were done in 1 mm glass capillaries (Hilgenberg, code 4007610, Germany) at RT, and the transmitted intensity data were recorded by a position-sensitive detector (PILATUS 300 K, Dectris). To cover the range of scattering vectors between 0.026 and 2 nm^{-1} ,

different detector positions were used. The circularly averaged data were normalized to incident beam, sample thickness, and measurement time before subtraction of the solvent. All measurements were put on an absolute scale by standard-less absolute intensity calibration.

SERS. Spectra were obtained using a Renishaw inVia reflex equipped with a stigmatic single-pass spectrometer, gratings of 1200 or 1800 grooves mm^{-1} , a Peltier-cooled CCD detector, a diode laser (785 nm, 300 mW) and a HeNe laser (633 nm, 17 mW) as excitation lines. Spectra were collected by focusing the laser spot below the air/liquid interface (z -position: $-500 \mu\text{m}$) of the sample liquid (200 μL) using either a 5x (Zeiss N PLAN, NA 0.12, WD 14 mm) or a 10x objective lens (Zeiss, NA 0.2). Each sample was measured in scanning mode for 10 s at least three times. For spectral assignment, SERS data was evaluated in reference to spectra of bulk materials (NTP, MUTAB, P(SS-co-MA), **Figure S14**) and analyte solutions of known concentrations ($[\text{NTP}] = 0.075 \text{ M}, 0.05 \text{ M}, 0.025 \text{ M}, 0.01 \text{ M}$, **Figure S15**) acquired by conventional volume Raman. Data analysis and background correction was done by multi-peak fitting using Igor Pro 7 (WaveMetrics, Inc., USA).

Heating experiments. Heating efficiency was determined by illuminating 1 mL of NP dispersion in a standard quartz cuvette from the side with a laser (fiber-coupled laser diode, Lumics LU0808T040) at 808 nm, as described by Roper *et al.*^{S8} The laser beam was collimated and expanded with lenses to form a spot that would cover the whole sample. In every case, the laser power illuminating the sample was 710 mW. Heating and cooling curves were then recorded by monitoring with a thermal imaging camera (FLIR A35), which was focused on the surface of the solution from above, at a distance of about 12 cm. Assemblies and nanorods were measured at three different concentrations, so an error bar representative of all experimental uncertainties could be obtained. The spheres were measured only once because, given their low absorbance at 808 nm, a highly concentrated sample (0.55 mM Au^0) was required to provide a thermal difference that can be accurately recorded ($\Delta T < 2 \text{ }^\circ\text{C}$). Finally, a sample containing only water was also measured to provide a background that excludes any heating contributions related to the medium.

Electromagnetic simulations. Extinction/absorbance/scattering spectra, induced electric fields, and surface charge distributions were calculated using a boundary element method (BEM) approach^{S9} using the MNPBEM toolbox^{S10} both in the quasi-static limit and including retardation effects, i.e., by solving the full Maxwell equations. The structures were represented by 144 vertices for spheres and $20 \times 20 \times 20$ vertices for rods, using a tabulated dielectric function representative for gold by Johnson and Christy from 400 to 1000 nm and a refractive index of 1.33 for water. Assemblies with disordered satellite distribution were modeled based on an algorithm following a random sequential adsorption mechanism. To account for the assembly variability, each morphological nanocluster species was represented by an averaged ensemble of 40 randomly assembled configurations.

Section ESI.1: Experimental optical properties and electron microscopy

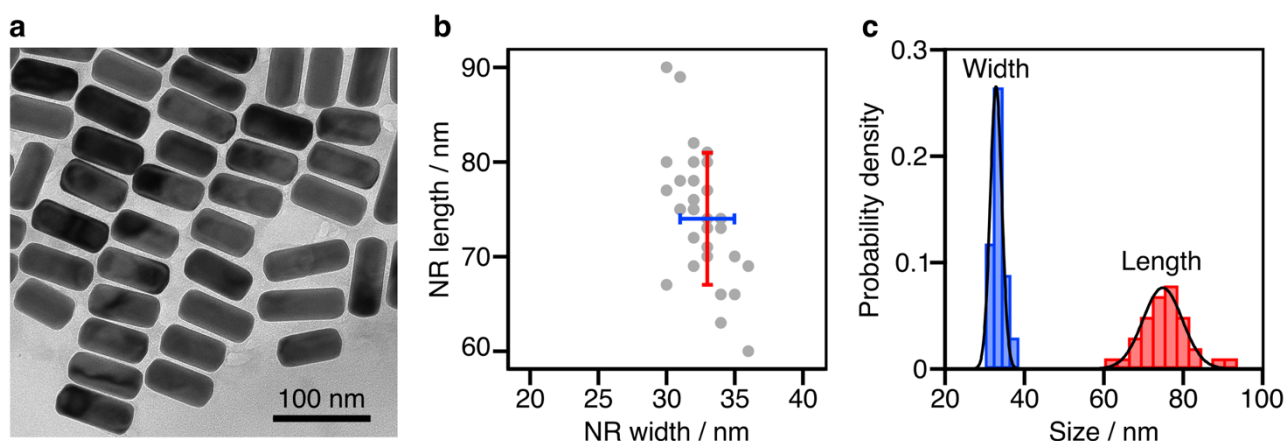


Figure S1. Size analysis of gold nanorods: (a) TEM image; (b) Correlation of length and width; (c) Histograms of sizes normalized to probability density. Average over 34 particles: length = 74 ± 7 nm, width = 33 ± 2 nm, AR = 2.2 ± 0.3 .

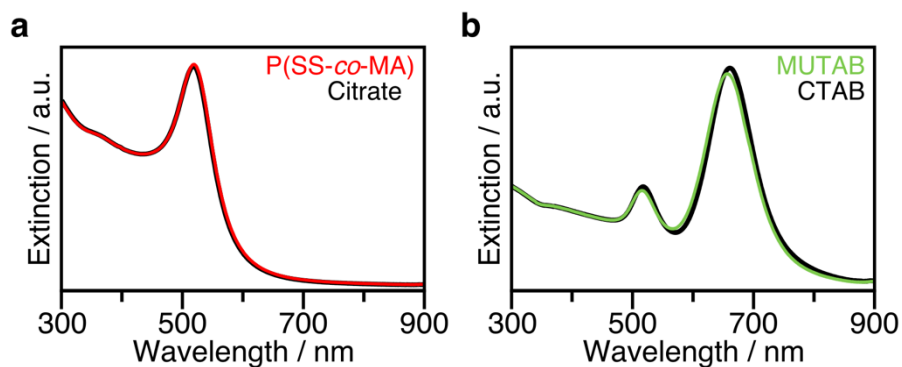


Figure S2. UV/vis/NIR extinction spectra of NP dispersions before (black) and after functionalization for assembly (red, green): (a) ligand-exchange of citrate against P(SS-co-MA) coating of nanospheres; (b) ligand-exchange of CTAB against MUTAB of nanorods. The extinction spectra before and after are identical except for a slight blue-shift of the longitudinal nanorod mode (661 nm) of 4 nm. This indicates adequate colloidal stability and the absence of aggregation.

Table S1. Optical changes by ligand-exchange as determined by UV/vis spectroscopy (**Figure S2**).

Sample	Function	LSPR / nm
AuNS16@citrate	--	521
AuNS16@P(SS-co-MA)	satellite NPs	521
AuNR@CTAB	--	661
AuNR@MUTAB	core NPs	657

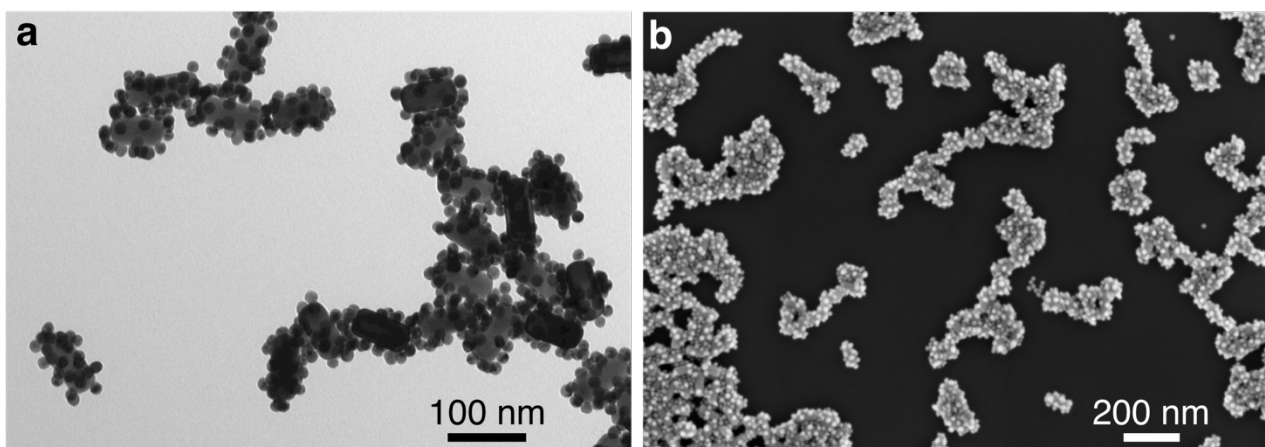


Figure S3. Electron microscopy images of dried dispersions of rods@spheres assemblies: (a) TEM of Cu grid; (b) SEM on Si wafer.

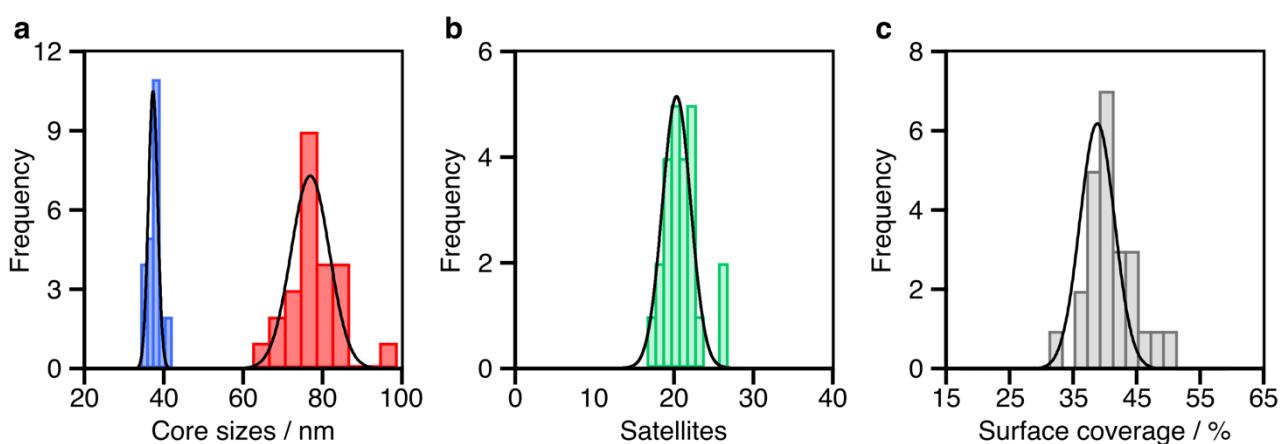


Figure S4. Estimation of satellite surface coverage by TEM image analysis of 24 assemblies: histograms and Gaussian regressions of (a) core width (blue) and length (red), (b) number of attached satellites (green), and (c) surface coverage of $39 \pm 4\%$, as calculated by Eq. S1.

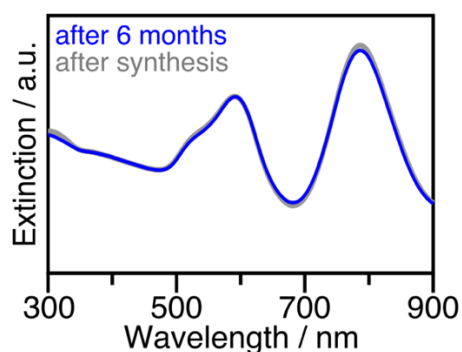


Figure S5. Long-term stability: UV/vis/NIR extinction spectra of NP dispersions of rod@spheres immediately after assembly (gray) and after 6 months of storage in a sealed vial at RT (dark blue). The plasmonic signature of the assemblies remains almost unchanged. This indicates that the net negative charge of the P(SS-co-MA) coating was sufficient to prevent aggregation over time. Only at the maximum of the coupling mode C_L around 800 nm minimal changes can be detected.

Section ESI.2: Quantification of radiative and non-radiative losses

The spectral losses of NP dispersions were quantified using a Cary 5000 spectrophotometer equipped with an external integrating sphere. A quartz glass cuvette was positioned at the center of the integrating sphere and a fixed set of measurements was performed:^{S1} sample measured without light trap (**Figure S6a-c**, green, scattered and transmitted light); sample measured with light trap (violet, scattered light); and water measured without light trap (gray, background). From this data, the spectral losses were evaluated. **Figure S6d-f** shows the extinction (black) as the sum of the transmittance of absorbed (blue) and scattered (red) light. Supported by electromagnetic simulations, an additional wavelength-independent scattering contribution was identified (**Figure S6d-f**, dotted lines). This becomes evident when looking at the results of the nanospheres of 15 nm in diameter (**Figure S6d**). For all samples, this background scattering amounts to approx. 3-5% related to the signal maximum. **Figure S6g-i** shows the corrected spectra after subtraction of the indicated scattering contributions.

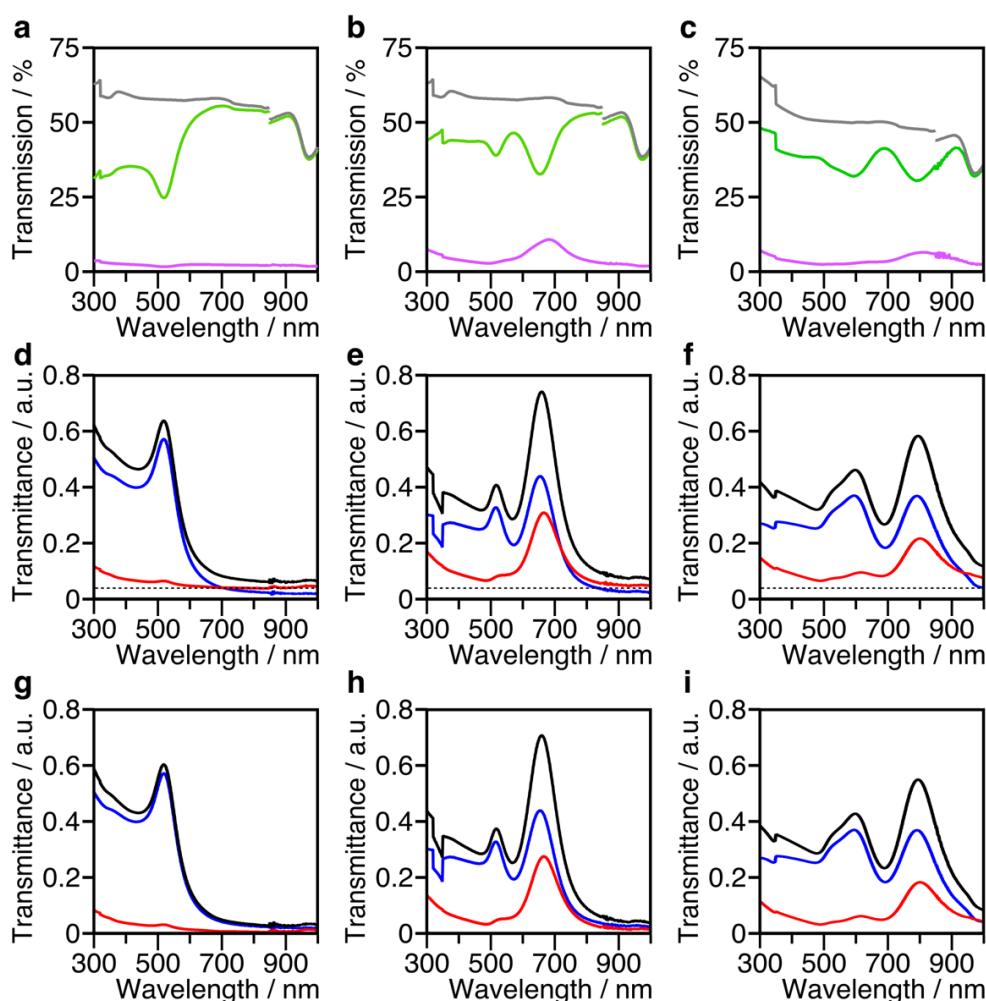


Figure S6. Characterization of spectral losses by diffuse reflectance spectroscopy of nanospheres (left), nanorods (middle), and rod@spheres assemblies (right): (a-c) Raw transmission intensity spectra of NP dispersions without (green) and with light trap (violet). Transmission intensity spectra of water, measured without light trap, serve as references (gray). (d-f) Evaluated transmittance spectra of radiative (red, scattering) and non-radiative (blue, absorption) losses. The total extinction is the sum of both contributions (black). (g-i) Baseline-corrected spectra by subtraction of wavelength-independent scattering contributions (dotted lines in d-f).

Section ESI.3: Structural characterization and 3D SAXS modeling

For *analytical* fitting, we used the open-source application *SasView* (<http://www.sasview.org>) and its implemented models. In all models, neither the ligand corona nor the polymer coating were considered in the analysis because of its negligibly low scattering contrast compared to gold. For *numerical* fitting, the scattering curves were calculated using the open-source software *Debyer* (<https://github.com/wojdyr/debyer>), which uses Debye's equation (see **Equation 1**). The scattering response was normalized with respect to $I(0)$ of the experimental data. The best fit was determined by a brute-force approach, for which, all parameter combinations of a reasonable parameter range were systematically calculated. The simulation resulted in two-dimensional maps, in which the best fit was selected by comparison with the mean square error (MSE) to the complete experimental scattering profile. The domain of lowest MSE was defined as a 10% deviation of the best possible fit to the experimental data (red area in **Figure 2b** and **S7b**).

Sphere model: The average radius of the satellite NPs was evaluated using the analytical model of a polydisperse spherical particle with its dispersity represented by a Gaussian distribution of radii.

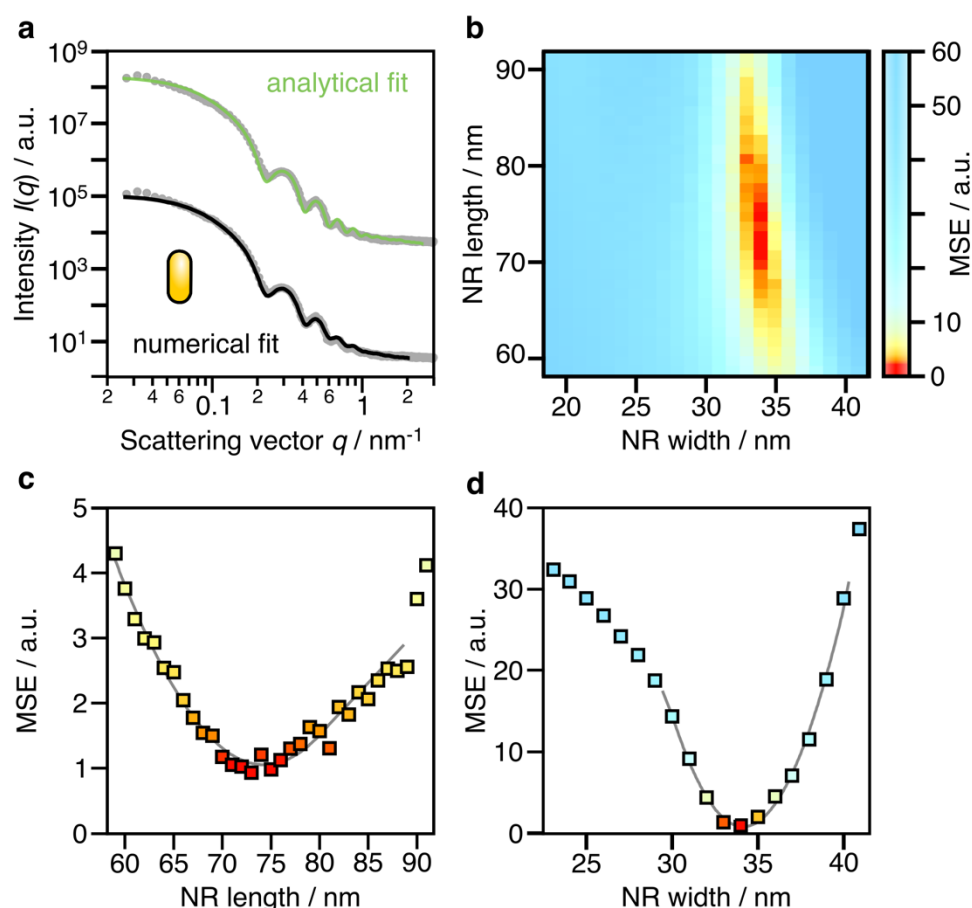


Figure S7. Structural characterization of core NPs (AuNRs): (a) Scattering curves (grey) and analytically (green, top) and numerically modeled data (black, bottom); offset applied for clarity. (b) MSE mapping of the free-parameter space by atomistic 3D modeling. Cross-sections for variations in length (c) and width (d) at the global minimum (domain of lowest MSE). The grey lines serve as guide-to-the-eye indications of the narrow range of the MSE minimum.

Nanorod model: The dimensions of the nanorod core could be accurately fitted by the analytical model of a homogenous cylinder with capped ends (**Figure 2a** and **S7a**, green). However, to validate our numerical approach (which will be employed to analyze the superstructures), the nanorod data was also evaluated using three-dimensional atomistic modeling.^{S1, S11, S12} For this purpose, the SAXS scattering curves were fitted numerically over the experimentally measured q -range of 0.03 to 0.8 nm⁻¹ (**Figure S7a**, black). Here, the nanorod was emulated by a cylinder with spherical caps consisting of randomly distributed scattering centers. The model features 4 independent parameters: length, length dispersity, width, and width dispersity. The dispersity was introduced by Gaussian-weighted averaging over a distribution of parameter sets (49 combinations per scattering curve). The MSE map in **Figure S7b** shows the independent parameters: length and width. The best-fit parameters, the domain of lowest MSE, show in red color as indicated by the logarithmic color scale. The high sensitivity of the SAXS response for morphological changes is illustrated in **Figure 2cd**. Each plot represents a cross section of the MSE map. The MSE of the NR width is highly sensitive ($\Delta\text{MSE}/\Delta\text{nm} > 1 \text{ nm}^{-1}$) and thus can be readily evaluated at nanoscale precision for a given NR length (**Figure S7d**). Compared to the width, the MSE of the NR length is less sensitive ($\Delta\text{MSE}/\Delta\text{nm} < 1 \text{ nm}^{-1}$) and the MSE minimum is less pronounced (**Figure S7c**). This is a clear indicator that the NR dispersity, even if it might be relatively low, should not be neglected in the following steps. All in all, the resulting parameters (length of 74±8 nm and width of 34±7 nm, see **Table S2**) were fully consistent with the analytical results and the TEM results (**Figure S1**), thus, validating our approach.

Table S2: Results of the structural analysis with fitting parameters are indicated by asterisks.

Model	Sphere	Nanorod	Assembly
Sphere radius / nm	7.5 ± 0.8 (*)	--	7.5
Nanorod length / nm	--	74 ± 11 (*)	74 ± 11
Nanorod width / nm	--	34 ± 4 (*)	34 ± 4
Satellite coverage / %	--	--	41 ± 5 (*)
Satellite number ^{a)}	--	--	18 ± 2 ^{b)}
Sat.-to-core distance / nm	--	--	1.5 ± 0.5 (*)

^{a)} Average number of satellite particles in an assembly with mean dimensions of 74 nm x 34 nm;

^{b)} Calculated value based on ensemble-averaged satellite coverage.

Assembly model: The morphology of the rod@spheres superstructures cannot be solved analytically, thus, it was necessary to develop a numerical model. This model builds on the afore evaluated parameters of the building block NPs (*vide supra*), which were held constant. The morphology of the assembly was described by 2 independent parameters (satellite coverage and core-to-satellite distance). The satellite coverage ($N_{\text{sat}}/N_{\text{max}}$) serves as a benchmark parameter and was defined as the surface coverage of satellite NPs compared to the total surface area of the rod core. The space requirement of a single satellite can be estimated by its spatial footprint (πr^2), given a non-curved surface of interaction. For the nanorod core, we make the assumption that its shape can be described by a cylinder segment ($\pi w (l-w)$) with two hemispherical caps (πw^2). This equates to

$$N_{\text{sat}}/N_{\text{max}} = N_{\text{sat}} (\pi r^2) / (\pi w (l-w) + \pi w^2) = N_{\text{sat}} (r^2) / (w l) \quad (\text{S1})$$

based on the number of satellites N_{sat} of radius r on a rod of length l and width w (cylinder of length $l-w$ capped by two half-spheres of diameter w). Here, N_{max} represents the hypothetical number of satellites that would cover the entire surface area (without leaving any free space). Please note that N_{max} does not represent close packing. For assemblies formed by random sequential adsorption (RSA),

the stochastic nature of the process limits the maximum surface coverage because of particle jamming. The jamming limit is the saturation coverage and depends on the local steric hindrances given by the respective geometrical situation. For example, the saturation coverage of a simple 2D assembly is about 0.547,^{S13,S14} which is considerably lower than hexagonal close-packing ($\pi/(3*2^{0.5}) \approx 0.74$). It has been shown that convex surface geometries can lead to lower steric hindrance between particles, and hence higher degrees of surface coverage per unit area.^{S14} This is because the higher curvature of the surface reduces the sterical hindrance. Consequently, reduced jamming could be expected at the tips of the nanorod as schematically depicted in **Figure S8**. In general, an analytical solution to the RSA adsorption is not feasible and therefore Monte Carlo (MC) simulations of the adsorption process need to be utilized. To account for this uncertainty, the scattering curves were calculated by averaging over 10 random satellite configurations with the respective geometrical (r , w , l) and structural parameters (N_{sat} and core-to-satellite distance ipd). Next, we will briefly estimate the effect of local surface jamming on anisotropic cores and discuss its possible influence on plasmonic coupling.

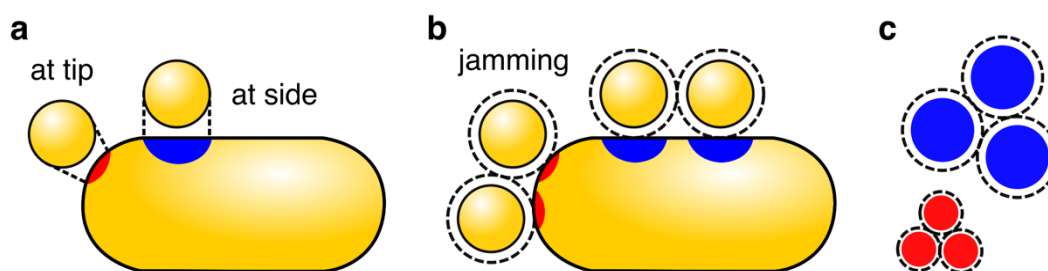


Figure S8. Position-dependent space requirement of spherical satellites on rod-shaped core: (a) Projection-based space requirement of spheres at the side (blue) and at the tips (red); (b) Surface jamming of closely-adjacent particle pairs. The dashed lines indicate the effective particle size accounting for the particle coating and repulsive interactions. (c) Simplified 2D projection of the differences in space requirement at the surface of three closely packed particles.

Local surface jamming on an anisotropic core: The space requirement of a satellite depends on its position at the rod surface. For instance, a sphere positioned at the side (blue) requires more space than at the tips (red); see **Figure S8a**. This causes a difference in jamming as it can be seen for pairs of particles (**Figure S8b**). The effective particle size is increased because of its coating and repulsive interactions (dashed lines). Consequently, a denser packing can be realized at the tips compared to the side (**Figure S8c**). The reduced footprint can be calculated by projecting a satellite onto a sphere of radius $w/2$. This projection corresponds to a spherical segment of height h and projected radius r_p with a surface area of $\pi(2r_p^2+h^2)$. The projected radius r_p is given by $r(w/2)/(w/2+r+ipd)$, where ipd is the gap size between core and satellite. Segment height h can be expressed by $(w/2)-((w/2)^2-r_p^2)^{0.5}$, which is the tip radius ($w/2$) minus the distance between segment base and tip center given by the Pythagorean equation. For the given parameters ($r/nm=7.5$, $w/nm=34$, $ipd/nm=1.5$), the space requirement at the tips can be estimated to be 13% lower compared to the (cylindrical) nanorod center section (152 nm^2 at tip vs. 177 nm^2 at side) so that the overall jamming limit would be about 6% higher. Considering the large number of influencing factors, this slight deviation can be neglected for reasons of simplicity. Please note that these simplified considerations should only point out that differences in core curvature affect the local jamming. It is not in our intent to claim that close packing is present in the studied system. At the same time, the proposed differences in jamming do not correspond to closer inter-particle distances - neither for the core-to-satellite distance, nor for the spacing between satellites. It is fair to assume that the inter-particle spacing is determined by the

steric hindrance of the particle coating and other repulsive interactions. Shorter distances would cause enhanced plasmonic coupling which makes the theoretical description more complex.

Section ESI.4: Electromagnetic simulations

The optical properties and electric-field confinement were modeled using electromagnetic simulations with the open-source *MNPBEM toolbox* by U. Hohenester and A. Trügler (<http://physik.uni-graz.at/mnpbem>). This toolbox is based on a boundary element method (BEM) approach developed by F. J. Garcia de Abajo and A. Howie.^{S9} In principle, it solves Maxwell's equations for a dielectric environment where nanoscale bodies with homogeneous and isotropic dielectric functions are separated by abrupt interfaces. As a first step, we modeled the optical properties of the building block NPs. Second, we developed a model for the assembly based on the random sequential adsorption (RSA) algorithm. Both steps were guided by the results of the structural analysis (see **Section ESI.3**).

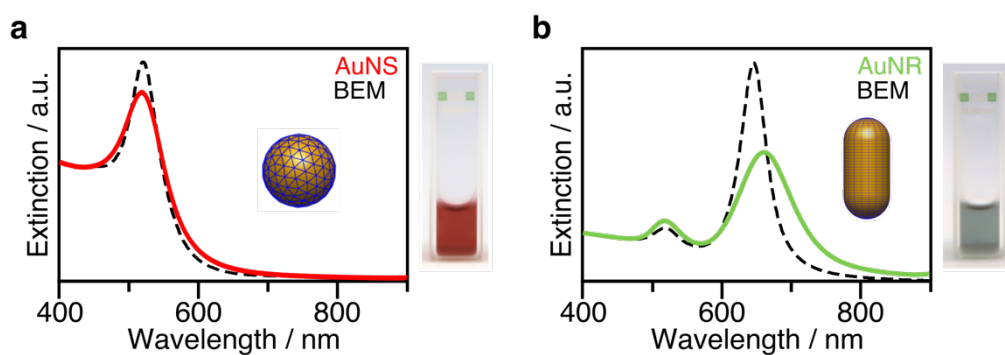


Figure S9. Optical properties of building block NPs: (a) nanospheres (AuNS@P(SS-co-MA), red); (b) nanorods (AuNR@MUTAB, green) in water. Dashed lines represent simulated spectra by BEM.

Modeling of the building block NPs: The calculation of the plasmonic properties of the building blocks is straight-forward and the obtained extinction spectra agree well with the experimental UV/vis/NIR results (**Figure S9**). For the simulations, the gold colloids were described by tabulated dielectric properties by Johnson and Christy^{S15} in a medium of a refractive index of 1.33. The nanospheres with a radius of 7.5 nm exhibit an LSPR maximum at 522 nm. The nanorods of 74 nm length and 34 nm width show maxima at 517 nm for the transversal mode and 644 nm for the longitudinal mode. The latter is known to be highly sensitive to morphological (shape, length, width, aspect ratio) and refractive index changes. For example, a minor increase in refractive index of 3% to $n=1.37$ has shown to shift the longitudinal LSRP to 655 nm.

Satellite distribution in assemblies: The models used to simulate the plasmonic responses of rod@spheres assemblies builds on the same RSA algorithm that was introduced in **Section ESI.3**. Briefly, a first satellite is placed randomly at the rod surface. Next, the coordinates of another satellite are randomly assigned but will only be accepted if the minimum distances to any other satellite, already present, are not below the threshold value of twice the core-to-satellite distance (emulating the satellite coating). The last step is repeated until the desired satellite coverage (in %) is achieved. For high coverages, sometimes finding a suitable solution can take quite long or might be ultimately futile. For that reason, we recommended to use a fail-safe check, that discards the previous coordinates if no further solution can be found (e.g., after 10^6 failed attempts).

Modeling of the assemblies in 3D and 2D: The plasmonic coupling within rod@spheres assemblies is complex. This complexity stems from the three-dimensional arrangement of the structure (**Figure S10ab**). To facilitate the evaluation of the distinct coupling contributions, we studied a simplified 2D model which limits the positioning of satellites to a single plane along the long axis of the rod core (**Figure S10cd**). Basically, the RSA algorithm generates disordered assemblies. With the help of certain geometrical restrictions, however, almost equidistant particle distances can be realized.

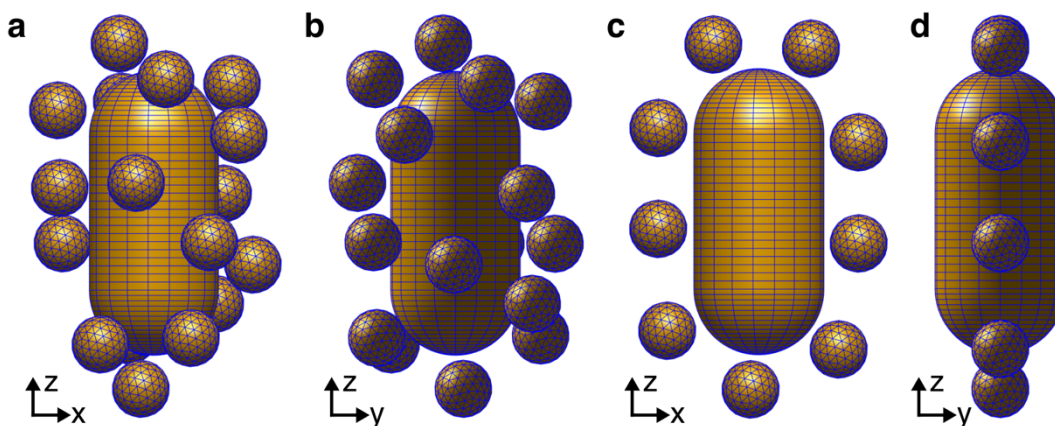


Figure S10. Exemplary models of rod@spheres assemblies: (a,b) Disordered 3D assembly of 18 randomly positioned spherical satellites on a rod core; (c,d) Simplified 2D assembly of 9 spherical satellites positioned in a plane along the long axis of the rod. In this specific example, the satellite spacing was chosen to be almost equidistant with a small distortion.

Distribution of surface charges and electric-field confinement: The excitation of the satellites mainly shows charge distributions which can be described by dipolar excitations. This can be explained by the fact that the dipolar contributions dominate in spherical particles of this size. To illustrate this, we calculated the surface charge distributions and plotted them onto the three-dimensional model (see **Figure 3** and **S13**). Here, the dipolar excitations of satellites were indicated by black arrows showing the orientation of the charge gradient as a guide-to-the-eye. Next, the induced fields can be calculated from the surface charges. Besides the induced fields (by the external excitation) also the contributions from the external field E_0 itself need to be considered. To obtain the total fields, both contributions are combined yielding E . The mapping of the electric-field confinement E/E_0 was performed for a plane along the long axis of the rod core.

Section ESI.5: Plasmonic coupling of multi-satellite assemblies

To discuss the plasmonic coupling of multi-satellite assemblies, we will first discuss the building blocks and the hybridization models of rod-sphere heterodimers (single-satellite assemblies) to predict the present dipole-dipole interactions. Based on this, we will compare the surface charge distributions simulated at the respective wavelengths, to examine if the characteristic requirements for bonding and anti-bonding hybridization are met. Because of anisotropy, it is necessary to discuss the system from different perspectives and polarizations.

Building blocks: Upon excitation along its long axis, the rod core (by itself) shows the characteristic dipolar charge distribution (R_L) which corresponds to the dominant mode of the extinction spectrum.

It should be noted that a phase shift and a corresponding charge reversal take place at the extinction maximum. Quite similar, for excitation along the other two principle axis (**Figure 3bc**), a transversal mode (R_T) appears. Although shown from two perspectives, it is in fact the same mode. A single nanosphere exhibits a dipolar mode at considerably higher energy. For an ensemble of satellites (S), a similar behavior can be seen in the absence of the rod core. The orbit of nanospheres shows that each particle is excited dipolarly by the external field. If the distances between the spheres were large enough, they would behave completely independent from each other. However, as shown in **Figure 3a**, a distance of about 1-2 radii suffices to cause a slight deflection of the particle polarization. For even shorter distances, the coupling becomes much stronger, as predicted by the plasmon ruler.^{S16,S17} For instance, at an inter-particle distance of 1 nm, the coupling mode can be expected at around 570 nm (**Figure S11**, red). However, 3 nm (i.e., 2x the particle coating) is more likely to describe the minimal inter-satellite spacing in the presented assemblies (**Figure S11**, orange). In any case, there is still a considerable energetic difference to the main rod mode (R_L).

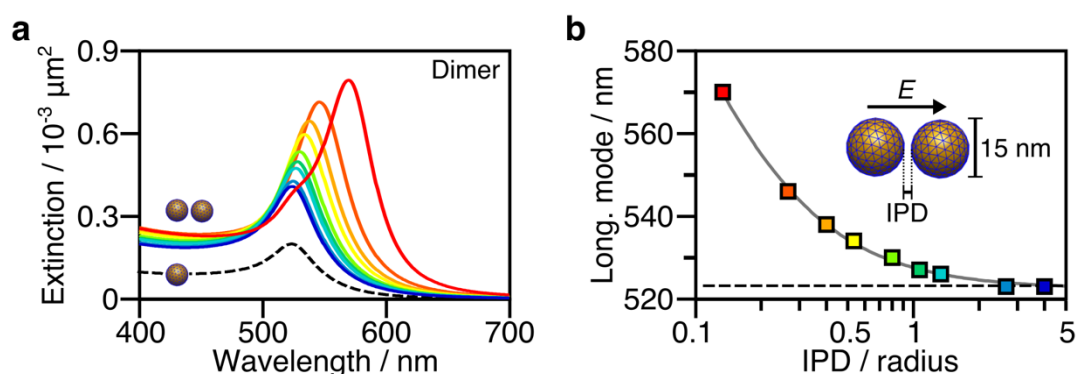


Figure S11. Gap-size dependent coupling of satellite homodimer (plasmon ruler): (a) Evolution of the calculated extinction spectra upon longitudinal excitation of two nanospheres of 7.5 nm in radius - for variation of the inter-particle gaps (IPD). (b) Longitudinal mode versus the gap size scaled in particle radii. The dashed lines correspond to a single nanosphere.

Plasmonic coupling of rod-sphere heterodimers (single-satellite assemblies): First, we consider hybridization in rod-sphere heterodimers because they represent the simplest building block of the assembly. Characteristic differences can be expected for the plasmon coupling between an Au nanorod and an Au nanosphere located at different positions of the nanorod.^{S18} This can be explained by the present dipole-dipole interactions, depending on the arrangement of the assembly axis \vec{A} (connection vector between the particle centers) to the polarization vector \vec{E} . **Figure S12a** schematically depicts the hybridization for longitudinal excitation (with respect to the nanorod). If the sphere is positioned at the tip of the rod, i.e. a parallel arrangement of dimer and polarization ($\vec{A} \parallel \vec{E}$), a rectified alignment of the dipoles is energetically advantageous (**Figure S12a**, left).^{S19} On the other hand, if the sphere is positioned on the side of the rod, i.e. a perpendicular arrangement of dimer and polarization ($\vec{A} \perp \vec{E}$), an antiparallel orientation of the dipoles is favorable (**Figure S12a**, right). Transverse excitation shows the analogous hybridization behavior (**Figure S12b**). Thus, it should be noted that the position of the satellite on the rod in relation to the excitation field is decisive whether an increase (rectified arrangement) or a decrease of the total net dipole moment (opposing arrangement of the dipoles) is energetically more favorable. Consequently, a reversal of the satellite dipole moment is necessary for a transition from tip to side or *vice versa* (**Figure S12cd**).^{S18} The increase in total net dipole moment by itself cannot be simply correlated with the mode type, bonding

or anti-bonding. According to the definition, the bonding mode describes an energetically favorable arrangement of the dipoles of the building components and the anti-bonding mode the energetically unfavorable one. In addition, this corresponds to a 180° reorientation of the satellite dipole moments at the characteristic locations (tip and side). This is not the case for the intermediate positions (**Figure S12cd**), because the anisotropy of the core causes the local charge distributions for longitudinal and transverse excitation to differ significantly. Thus, the reversal of the satellite dipole moment (change in orientation per spatial dislocation)^{S18} is not the same for both polarizations.

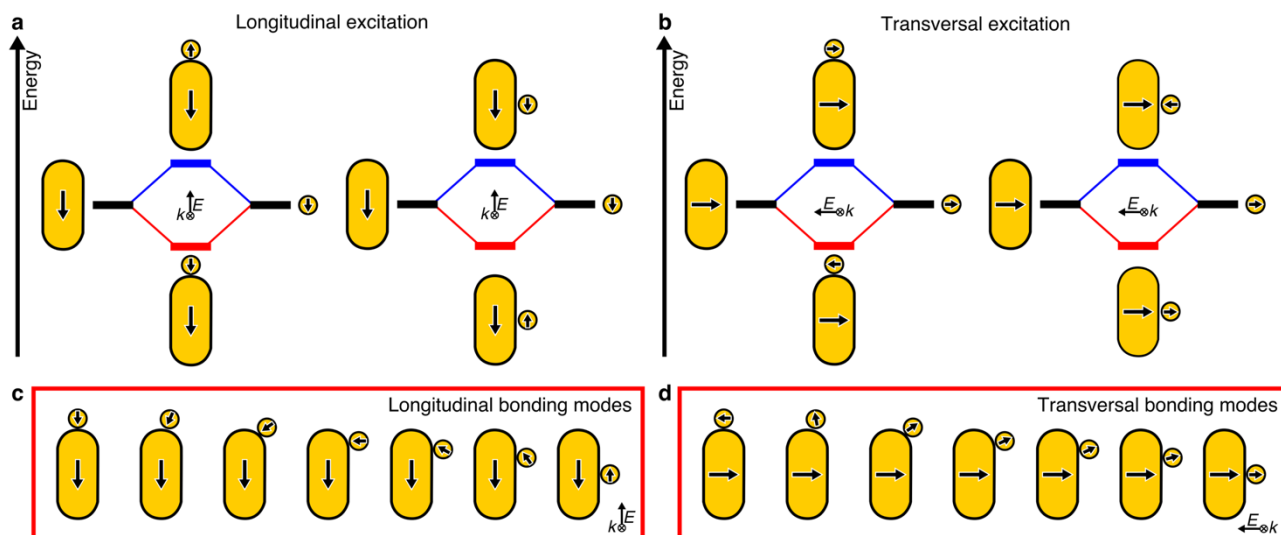


Figure S12. Plasmonic coupling of rod-sphere heterodimers for (a,c) longitudinal and (b,c) transversal excitation (in respect to the rod). (a,b) Schematic hybridization models for sphere-at-tip and sphere-at-side geometries with the orientations of induced dipoles indicated by black arrows. Bonding modes show energetically favorable dipole-dipole configurations (red) while anti-bonding modes show energetically unfavorable ones (blue). (b,d) The transition from tip to side position is accompanied by a reorientation of the dipoles.^{S18} The relative orientations at intermediate positions depend on the local distribution of charges and is depicted as a guide to the eye.

Plasmonic coupling of multi-satellite assemblies for polarization along the long axis ($\vec{A}||\vec{E}$): The multi-satellite structure shows a mode splitting (**Figure 3d**, black line) yielding a dominant excitation at lower energy (780-800 nm, C_L) and a very weak secondary excitation (520-540nm, C_L^*), energetically just below the satellite orbit (S). The dominant mode can be assigned to the energetically favorable bonding mode C_L . The corresponding surface charge plots show that the satellites exhibit dipole moments aligned toward the core charges, yielding an energetically favorable overall charge distribution (**Figure S13a**, red box). This agrees with the expectations based on the fundamental hybridization behavior (see scheme). An alternative description is that the satellites do not become polarized by the external field directly but by the induced electric field of the rod core, i.e., its surface charges. Consequently, the C_L mode appears at higher wavelengths and is red-shifted to the core mode R_L . The weak second mode could represent the antibonding mode C_L^* , which is energetically unfavorable and would be expected at higher energies. The simulated surface charges (**Figure S13a**, blue box) show an arrangement of the satellite dipoles as expected (see scheme). However, the rod core does not show a single dipolar but more complex charge distribution. Also, the charge pattern of the rod core is rather weak compared to the satellites. This might indicate destructive interferences between the antibonding mode and other modes (possibly higher order^{S18,S20}).

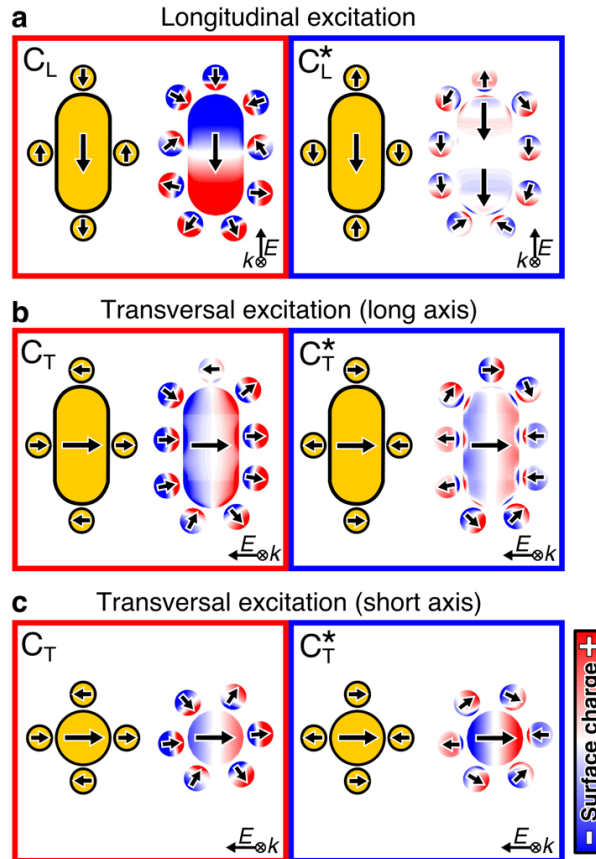


Figure S13. Plasmonic coupling of anisotropic core/satellite superstructures: Surface charge density plots of simplified 2D assemblies in comparison to basic dipole-dipole interactions (schematics) according to hybridization theory, in the three principal planes of excitation: (a) longitudinal, (b) transversal along long axis and (c) transversal along short axis of the rod core. The dipole-dipole orientations of the coupled modes agree well with expectation of the fundamental bonding (C) and anti-bonding (C*) modes of arrangements with satellites at the tips and sides of the rod core.

Plasmonic coupling of multi-satellite assemblies for polarization along the short axis ($\vec{A} \perp \vec{E}$): For transversal excitation, the multi-satellite structure shows a less-pronounced mode splitting (**Figure 3e**, black line) yielding a dominant mode at lower energy (600-650nm, C_T) and secondary excitation at higher energy (520-540nm, C_T^*) close to the energetic levels of rod (R_T) and satellite orbit (S). Again, we compare the surface charge distributions to expectations from hybridization theory (**Figure S13b**). Here, the orientation of the satellites is in good agreement with the presumed dipole-dipole interactions (see schemes). For both the bonding (C_T , red box) and anti-bonding mode (C_T^* , blue box), the reorientation of the satellite for the intermediate locations between tip and side is clearly visible. Thus, we can safely assign the dominant low energy mode (600-650nm) to be of bonding type and the higher energy mode (520-540nm) to be of anti-bonding type. For a transversal excitation from the perspective at the rod ends, we find an even less pronounced mode splitting (**Figure 3e**). This can be explained by the smaller number of satellites. The energetically lower mode (580-610nm) shows a surface charge pattern in agreement with a bonding-type mode (**Figure S13c**, red box). Similarly, the energetically higher mode (520-540nm) shows a surface charge pattern according to expectations for an antibonding-type mode (**Figure S13c**, blue box).

Section ESI.6: Analysis of SERS data and reference Raman spectra

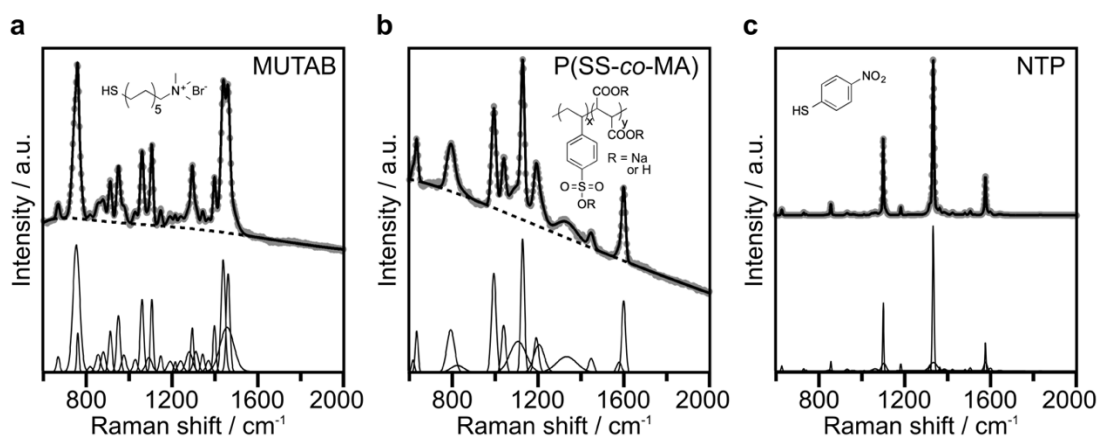


Figure S14: Reference Raman spectra of (a) MUTAB, (b) P(SS-co-MA), and (c) NTP; all in dry state. Raw spectra (grey dots), modeled data (black), baselines (dashed black), and spectral deconvolutions by multi-peak fitting (bottom).

Figure S14 depicts Raman measurements of the chemicals MUTAB, P(SS-co-MA), and NTP used for coating and labeling. **Figure S15** shows the Raman measurements of NTP solutions in EtOH of reference concentrations. The intensity of the characteristic signals νNO_2 and $\nu\text{CC,ar.}$ increase linearly with the concentration of NTP. The indicated error bars refer to the uncertainty of background correction and spectral deconvolution. The aromatic signals are highly correlated. The non-resonant Raman cross-section of NTP at 633 nm (**Figure S15a**) is higher than at 785 nm (**Figure S15b**). The signal intensities were determined by spectral deconvolution (multi-peak fitting). The background was corrected by a log-cubic baseline function, which is principally a polynomial in $\log(x)$ instead of x (cubic function with 4 non-zero parameters). Please note, to obtain quantitative data for aqueous NTP solution containing EtOH as solubilizing agent, special care is required as evaporation (loss of EtOH) will influence the concentration of the Raman reporter. For this purpose, the time between sample preparation and SERS measurement was kept constant for all samples.

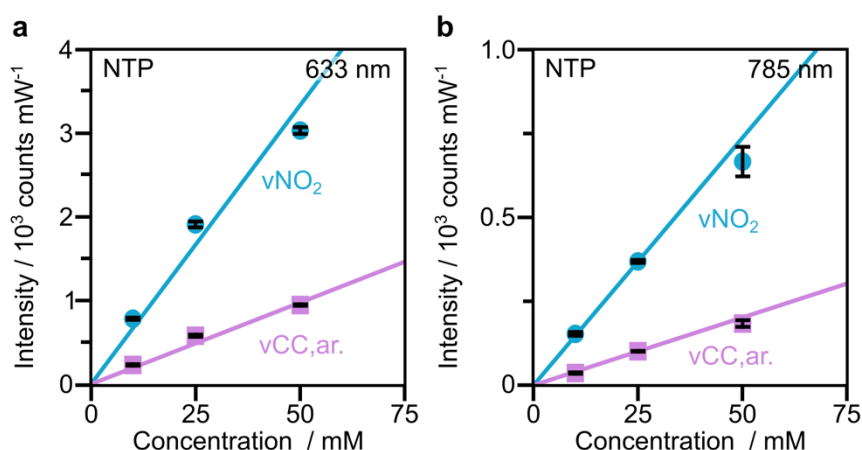


Figure S15: Raman intensities of νNO_2 (cyan) and $\nu\text{CC,ar.}$ signals (violet) of reference concentrations of NTP (0 mM, 10 mM, 25 mM, and 50 mM) excited at (a) 633 nm and (b) 785 nm. Raman cross-sections derived from the concentration-dependent intensity: (a) νNO_2 (66.50 ± 0.63) $\times 10^3$ counts $\text{mW}^{-1} \text{mM}^{-1}$; $\nu\text{CC,ar.}$ (19.48 ± 0.15) $\times 10^3$ counts $\text{mW}^{-1} \text{mM}^{-1}$; (b) νNO_2 (14.77 ± 0.15) $\times 10^3$ counts $\text{mW}^{-1} \text{mM}^{-1}$, $\nu\text{CC,ar.}$ (4.05 ± 0.04) $\times 10^3$ counts $\text{mW}^{-1} \text{mM}^{-1}$.

Section ESI.7: Calculation of the enhancement factor and surface coverage of NTP

The analytical enhancement factor (AEF)^{S21,S22} can be calculated by **Equation 2**. Based on the non-enhanced Raman cross-sections (see **Figure S15**), a signal enhancement of approx. 10^5 could be calculated (**Table S3**). Here, the maximum number of adsorbed analyte molecules on the assemblies is crucial because **Equation 2** is only valid for a sub-monolayer of adsorbed NTP molecules.

Table S3: Evaluation of SERS enhancement and efficiency.

Excitation line / nm	633	633	785	785
Laser power / mW	6.6	6.6	70	70
c_{Au^0} / μM	0.25	0.25	0.25	0.25
Raman mode	NO ₂	CC,ar.	NO ₂	CC,ar.
I_{SERS} / counts	9,889±43 (1h)	3,325±49 (1h)	106,060±550 (1h)	20,590±280 (1h)
	--	--	126,570±2,570 (1d)	24,970±340 (1d)
	--	--	125,510±2,360 (4d)	24,850±310 (4d)
c_{SERS} / M	1×10^{-6}	1×10^{-6}	1×10^{-6}	1×10^{-6}
$I_{RS} c_{RS}^{-1}$ / counts mM ⁻¹	439±5	129±1	1034±11	283±3
SERS enhancement (AEF) / 10^5	0.23±0.01 (1h)	0.26±0.01 (1h)	1.03±0.02 (1h)	0.73±0.02 (1h)
	--	--	1.22±0.03 (1d)	0.88±0.02 (1d)
	--	--	1.21±0.03 (4d)	0.88±0.02 (4d)
SERS efficiency (AEF/ c_{Au}) / 10^5 mM ⁻¹	0.92 (1h)	1.04 (1h)	4.12 (1h)	2.92 (1h)
	--	--	4.88 (1d)	3.52 (1d)
	--	--	4.84 (4d)	3.52 (4d)

Table S4: Estimated values for the calculation of the sub-monolayer of NTP.

Sample	Assemblies	Only satellites	Only cores
Satellite size / nm	15	15	--
Core size (length x width) / nm x nm	74 x 34	--	74 x 34
Satellite coverage / average satellites per core	18	18	--
Surface area / nm ²	20,630	18x 707 = 12,726 (62%)	7,904 (38%)
Volume / nm ³	88,702	18x 1,767 = 31,806 (36%)	56,896 (64%)
Particle conc. for 0.25 mM Au ⁰ / NPs L ⁻¹	2.87×10^{13}	51.66×10^{13}	2.87×10^{13}
Total surface area / nm ² per L	5.93×10^{17}	3.65×10^{17}	2.27×10^{17}
Max. number of adsorbed NTP molecules per L	2.79×10^{18}	1.72×10^{18}	1.07×10^{18}
Maximum number of adsorbed NTP / M	4.63×10^{-6}	2.86×10^{-6}	1.77×10^{-6}

Maximum number of adsorbed NTP molecules: The saturation limit for the absorption of NTP can be estimated based on the assemblies' surface area of gold. Here, we take into account the sizes and satellite coverage (number of satellite NPs per core NP) obtained by TEM and SAXS (see **Section ESI.1** and **ESI.3**). The total available metallic surface area of an individual rod@spheres assembly (18 satellites in average) equates to approximately 20,630 nm². A gold concentration of 0.25 mM Au⁰ corresponds to a particle concentration of 2.87×10^{13} assemblies per liter. Thus, the metallic surface in 1 L is approximately 5.93×10^{17} nm² L⁻¹ or 0.6 m² L⁻¹ (see **Table S5**). Thiophenol-derived analyte molecules like NTP are known to form self-assembled monolayers on flat Au surfaces with a density of about 4.7 molecules nm⁻².^{S23,S24} Consequently, the maximum number of NTP molecules that could be adsorbed is about 2.79×10^{18} molecules L⁻¹ or 4.63×10^{-6} M. Because the final NTP concentration was 1.0×10^{-6} M in the SERS experiments (see **Section ESI.0**) it is safe to assume a sub-monolayer of NTP at the Au surface, even for a quantitative adsorption of NTP. In addition, this concentration is also below the theoretical saturation limits for an exclusive absorption on either the core NPs (1.77×10^{-6} M) or the satellite NPs (2.86×10^{-6} M).

Table S5. Spectral assignment of the observed Raman shifts based on literature values and reference spectra of NTP, P(SS-co-MA), MUTAB, and water.

Raman shift / cm ⁻¹	Vibrational assignment	Molecule assignment	Ref.
329, 531	Ring deform.	NTP	S25
723, 733	vCS stretch.	NTP	S25
820 (s), 856 (m)	vCN stretch. or vCH wag.	NTP	S25
1061, 1081 (m), 1109 (s), ^{a)} 1178 (m), 1367	vCH bend.	NTP	S25
1109 (s) ^{a)}	vCS ^{a)}	NTP ^{a)}	S26,S27
1330 (s)	vNO ₂ , sym.	NTP	S25,S28
1430, 1468, 1488	Ring stretch.	NTP	S25
1567 (s)	vCC,ar. stretch.	NTP	S25,S28
618	dOCO	MA of P(SS-co-MA)	S29
~	dSO ₃	SS of P(SS-co-MA)	S30
635	dSO ₃	SS of P(SS-co-MA)	S30
793	dOCO	MA of P(SS-co-MA)	S29
~	vCS	SS of P(SS-co-MA)	S30
825	vCS	SS of P(SS-co-MA)	S30
995	vCC,ar. stretch., breathing	SS of P(SS-co-MA)	S30
1041	vSO ₃ ²⁻ sulfonate ion	SS of P(SS-co-MA)	S30
1108	vC-OH	MA of P(SS-co-MA)	S29
~	vSO	SS of P(SS-co-MA)	S30
1129	vCC,ali.	MA of P(SS-co-MA)	S29
~	vSO ₂ sulfone	SS of P(SS-co-MA)	S30
1193	dCH, dCH ₂	SS of P(SS-co-MA)	S30
~	vSO	MA of P(SS-co-MA)	S29
1205, 1334	dCH, dCH ₂	MA of P(SS-co-MA)	S29
1334	vOCO,sym.	MA of P(SS-co-MA)	S29
1449	vCH ₂ beta	MA of P(SS-co-MA)	S29
1578	vOCO,asym.	MA of P(SS-co-MA)	S29
1600	vCH,ar. quadrant stretch.	SS of P(SS-co-MA)	S30
754, 760	vCN ⁺	MUTAB	S31,S32
912, 950, 976	--	MUTAB	--
1029, 1061 (s), 1093, 1106 (s), 1148, 1191	vCC,ali., skeletal	MUTAB	S31-S33
1215, 1240, 1370	vCH ₂ , wag.	MUTAB	S12,S31,S33
1281, 1295, 1312, 1343, 1298, 1439, 1457, 1462	vCH ₂	MUTAB	S31-S33
1295	vCH ₃ twisting	MUTAB	S33
1370	vCH ₃ deformation	MUTAB	S33
1457	vCH ₃ scissoring	MUTAB	S33
2422	vSH	MUTAB	--
1581, 1641	vOH bending	H ₂ O	S34

^{a)} In the literature, contradicting assignments concerning this signal can be found.

Section ESI.8: Plasmonic heating experiments

The heating efficiency, η , relates the energy balance of the system to the fraction of attenuated light:

$$\eta = \frac{Q_{\text{sample}} - Q_{\text{medium}}}{P (1 - 10^{-\text{Ext}808})} \quad (\text{S2})$$

In **Equation S2**, P is the laser power and $\text{Ext}808$ denotes the optical density (extinction) of the sample at the laser wavelength. Thus, the denominator accounts for the income energy. Q_i accounts for the energy delivered by either the sample or the medium, and is defined as $m_i C_{\text{sample}} \Delta T / \tau$, where m is the mass, C_{sample} is the heat capacity of the sample (that can be approximate as water in our experiment), ΔT is the thermal increment of the sample when equilibrium is reached, and τ is the time constant that gives the transient temperature curve. This last parameter quantifies the energy exchange with the surroundings, which is more accurately measured from the cooling curve. Accordingly, the experimental procedure involves illuminating the sample until the temperature stabilizes to get ΔT , then the illumination is turned off to let the cooling cycle start. **Figure S16** shows as an exemplary cooling curve of a dispersion of nanorods. The exponential fit to the data corresponds to a time constant τ of 237 s (note the logarithmic scale).

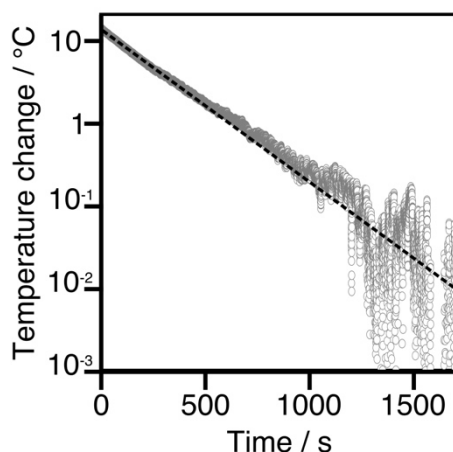


Figure S16. Exemplary cooling curve of a dispersion of nanorods with an exponential regression (dashed black line).

ESI References

- S1 R. P. M. Höller, M. Dulle, S. Thomä, M. Mayer, A. M. Steiner, S. Förster, A. Fery, C. Kuttner and M. Chanana, *ACS Nano*, 2016, **10**, 5740–5750.
- S2 M. Karg, I. Pastoriza-Santos, J. Pérez-Juste, T. Hellweg and L. M. Liz-Marzán, *Small*, 2007, **3**, 1222–1229.
- S3 M. Tebbe, C. Kuttner, M. Mayer, M. Maennel, N. Pazos-Perez, T. A. F. König and A. Fery, *J. Phys. Chem. C*, 2015, **119**, 9513–9523.
- S4 M. Mayer, A. M. Steiner, F. Röder, P. Formanek, T. A. F. König and A. Fery, *Angew. Chem., Int. Ed.*, 2017, **56**, 15866–15870.
- S5 N. G. Bastús, J. Comenge and V. Puntes, *Langmuir*, 2011, **27**, 11098–11105.

- S6 J. Rodríguez-Fernández, J. Pérez-Juste, P. Mulvaney and L. M. Liz-Marzán, *J. Phys. Chem. B*, 2005, **109**, 14257–14261.
- S7 T. Hendel, M. Wuithschick, F. Kettemann, A. Birnbaum, K. Rademann and J. Polte, *Anal. Chem.*, 2015, **87**, 5846–5847.
- S8 D. K. Roper, W. Ahn and M. Hoepfner, *J. Phys. Chem. C*, 2007, **111**, 3636–3641.
- S9 F. J. Garcia de Abajo and A. Howie, *Phys. Rev. B*, 2002, **65**, 115418.
- S10 U. Hohenester and A. Trügler, *Comput. Phys. Commun.*, 2012, **183**, 370–381.
- S11 M. J. Schnepf, M. Mayer, C. Kuttner, M. Tebbe, D. Wolf, M. Dulle, T. Altantzis, P. Formanek, S. Förster, S. Bals, T. A. F. König and A. Fery, *Nanoscale*, 2017, **9**, 9376–9385.
- S12 C. Kuttner, M. Mayer, M. Dulle, A. Moscoso, J. M. López-Romero, S. Förster, A. Fery, J. Pérez-Juste and R. Contreras-Cáceres, *ACS Appl. Mater. Interfaces*, 2018, **10**, 11152–11163.
- S13 P. Schaaf and J. Talbot, *J. Chem. Phys.*, 1989, **91**, 4401–4409.
- S14 B. M. Manzi, M. Werner, E. P. Ivanova, R. J. Crawford and V. A. Baulin, *Sci. Rep.*, 2019, **9**, 780.
- S15 P. B. Johnson and R. W. Christy, *Phys. Rev. B*, 1972, **6**, 4370–4379.
- S16 N. Liu, M. Hentschel, T. Weiss, A. P. Alivisatos and H. Giessen, *Science*, 2011, **332**, 1407–1410.
- S17 C. Sönnichsen, B. M. Reinhard, J. Liphardt and A. P. Alivisatos, *Nat. Biotechnol.*, 2005, **23**, 741–745.
- S18 L. Shao, C. Fang, H. Chen, Y. C. Man, J. Wang and H.-Q. Lin, *Nano Lett.*, 2012, **12**, 1424–1430.
- S19 L. V. Brown, H. Sobhani, J. B. Lassiter, P. Nordlander and N. J. Halas, *ACS Nano*, 2010, **4**, 819–832.
- S20 P. Nordlander, C. Oubre, E. Prodan, K. Li and M. I. Stockman, *Nano Lett.*, 2004, **4**, 899–903.
- S21 E. C. Le Ru and P. G. Etchegoin, *Mrs Bull.*, 2013, **38**, 631–640.
- S22 E. C. Le Ru, E. Blackie, M. Meyer and P. G. Etchegoin, *J. Phys. Chem. C*, 2007, **111**, 13794–13803.
- S23 H. Kang, H. Lee, Y. Kang, M. Hara and J. Noh, *Chem. Commun.*, 2008, **41**, 5197–5199.
- S24 A. Le Beulze, S. Gomez-Grana, H. Gehan, S. Mornet, S. Ravaine, M. Correa-Duarte, L. Guerrini, R. A. Alvarez-Puebla, E. Duguet, E. Pertreux, A. Crut, P. Maioli, F. Vallée, N. Del Fatti, O. Ersen and M. Tréguer-Delapierre, *Nanoscale*, 2017, **9**, 5725–5736.
- S25 B. O. Skadtchenko and R. Aroca, *Spectrochim. Acta A*, 2001, **57A**, 1009–1016.
- S26 Y. Ling, W. C. Xie, G. K. Liu, R. W. Yan, D.-Y. Wu and J. Tang, *Sci. Rep.*, 2016, **6**, 120.
- S27 B. Dong, Y. Fang, L. Xia, H. Xu and M. Sun, *J. Raman Spectrosc.*, 2011, **42**, 1205–1206.
- S28 B. M. Devetter, P. Mukherjee, C. J. Murphy and R. Bhargava, *Nanoscale*, 2015, **7**, 8766–8775.
- S29 J. L. Castro, M. R. López-Ramírez, J. F. Arenas and J. C. Otero, *Vib. Spectrosc.*, 2005, **39**, 240–243.
- S30 H. G. M. Edwards, D. R. Brown, J. A. Dale and S. Plant, *Vib. Spectrosc.*, 2000, **24**, 213–224.
- S31 M. Tebbe, C. Kuttner, M. Männel, A. Fery and M. Chanana, *ACS Appl. Mater. Interfaces*, 2015, **7**, 5984–5991.
- S32 S. Lee, L. J. E. Anderson, C. M. Payne and J. H. Hafner, *Langmuir*, 2011, **27**, 14748–14756.
- S33 A. L. Dendramis, E. W. Schwinn and R. P. Sperline, *Surf. Sci.*, 1983, **134**, 675–688.
- S34 D. M. Carey and G. M. Korenowski, *J. Chem. Phys.*, 1998, **108**, 2669–2675.